Electronic Supplementary Material (ESI) for Energy & Environmental Science.

Electronic Supplementary Information

Evaluating Particle-Suspension Reactor Designs for Z-Scheme Solar Water Splitting via Transport and Kinetic Modeling

Rohini Bala Chandran,[1] Sasuke Breen,[2] Yuanxun Shao,[3] Shane Ardo,[2,3,]*
and Adam Z. Weber[1,]*

1. Dimensioning the Porous Separator

Applying one-dimensional Fick's law of diffusion in the porous separator and assuming saturated concentrations of H_2 and O_2 (1.23 mM for H_2 and 0.78 mM for O_2) in alternate reaction compartments yields the diffusive flux of the dissolved gas species,

$$N_i = \frac{w_{sep}\varepsilon_{sep}D_i c_{sat,i}}{t_{sep}w_{unit}} \tag{1}$$

where, i corresponds to dissolved H_2 or O_2 species, w_{sep} is the separator width, ε_{sep} is the separator porosity, D_i is dissolved gas diffusivity ($D_{H_2,\infty} = 5.11 \times 10^{-5}$, $D_{O_2,\infty} = 2.42 \times 10^{-5}$ $cm^2\ s^{-1}$), $c_{sat,i}$ is the saturated species concentrations in water, t_{sep} is the separator thickness and w_{unit} is the unit cell width. To achieve crossover losses less than 2% [1] relative to the hydrogen production rates at 1% baseline STH efficiency,

$$\frac{N_{H_2}}{N_{H_2,baseline}} < 0.02 \tag{2}$$

where, $N_{H_2,baseline} =$ 8.43×10^{-5} mol m^{-2} s^{-1}. Combining eqs. (1) and (2) leads to the constraint of $\frac{w_{sep}\varepsilon_{sep}}{w_{unit}} < 0.21$ for an assumed separator thickness of $t_{sep} = 1$ mm.

2. Optical Properties

Figure S1 shows the optical absorption coefficients of the semiconductor particles, redox shuttles and water based on reported data in the literature [2–8]. Cabrera et al. [2] provide experimental measurements for the absorption cross-sections of colloidal suspensions of TiO_2 and optical properties of $BiVO_4$ and $SrTiO_3$:Rh powders

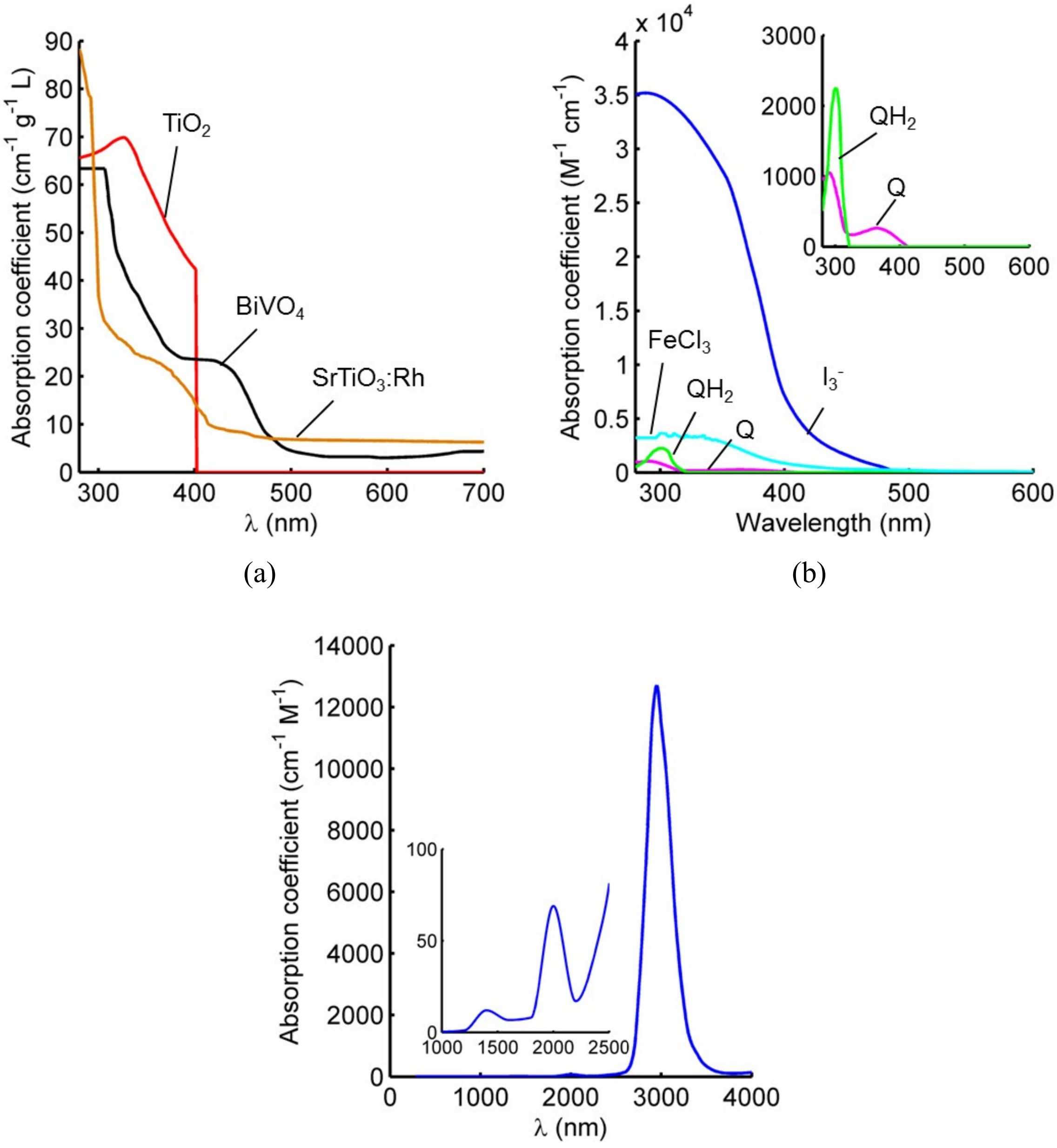

(a) (b)

(c)

Figure S1. Spectral absorption coefficients for the considered (a) semiconductor particles (b) redox shuttles and (c) water at ambient temperature of 298.15 K

are obtained from [3] and [4], respectively. In all these cases, the particle/agglomerate sizes considered in these studies were on the order of hundreds of nanometers and therefore, reasonable to be applied in our study of particles with an average particle/agglomerate size of 100 nm. For TiO_2, absorption data has been provided in ref. [2] only for wavelengths less than 400 nm. It is assumed that TiO_2, which has a band gap of 3.1 eV (wavelength equivalent of 400.2 nm), is transparent for the longer wavelengths; only incident photons with energies higher than the band gap are absorbed by the TiO_2 particles in the suspension. The molar absorption coefficients for the redox shuttles are obtained from the literature [5–7], except for $FeCl_3/FeCl_2$, which were experimentally evaluated in-house with an Agilent Cary 60 UV-VIS spectrophotometer. The absorbance of a wetted dialysis membrane (Spectra/Por® 3 Regenerated cellulose dialysis membrane) was also evaluated experimentally and Figure S2 indicates that the absorbance values are rather low in the visible region (400 – 900 nm). Therefore, it is reasonable to neglect the light intensity attenuation by the porous separator in our calculations even for the 1 mm thick separators.

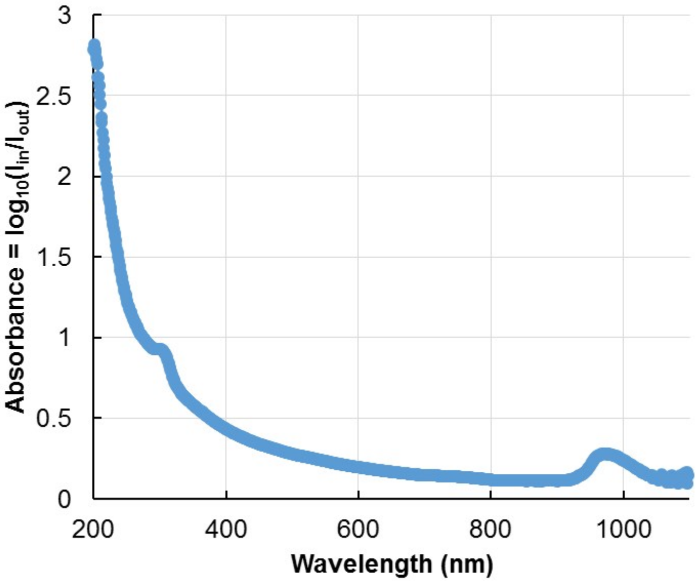

Figure S2 Spectral absorbance values measured for a wetted dialysis membrane with an average thickness of about 0.4 mm.

3. Results

Effects of Optical Properties

The impacts of the particle optical thicknesses on the reaction rates in the bottom HER compartment with $SrTiO_3$:Rh particles is shown in Figure S3 for various concentrations of the Q/QH_2 redox shuttle. For both Option I and Option II, the decrease in the reaction rates due to increase in the redox shuttle concentration is more pronounced when the OER particle optical thicknesses are small, $\tau_{p,top} < 0.1$. For the larger OER particle optical thicknesses, the reaction rate is limited more by attenuation of incident light by the $BiVO_4$ particles in the top compartment than by the redox shuttle. The bottom compartment reaction rates are less influenced by the optical thicknesses of the TiO_2 particles as compared to the $BiVO_4$ particles due to tandem light absorption of the relatively higher energy photons by the TiO_2 particles (Option I). For both options, the maximum bottom compartment reaction rate reduces by as much as 20% when the redox shuttle concentration increases from 10^{-3} M to 0.1 M.

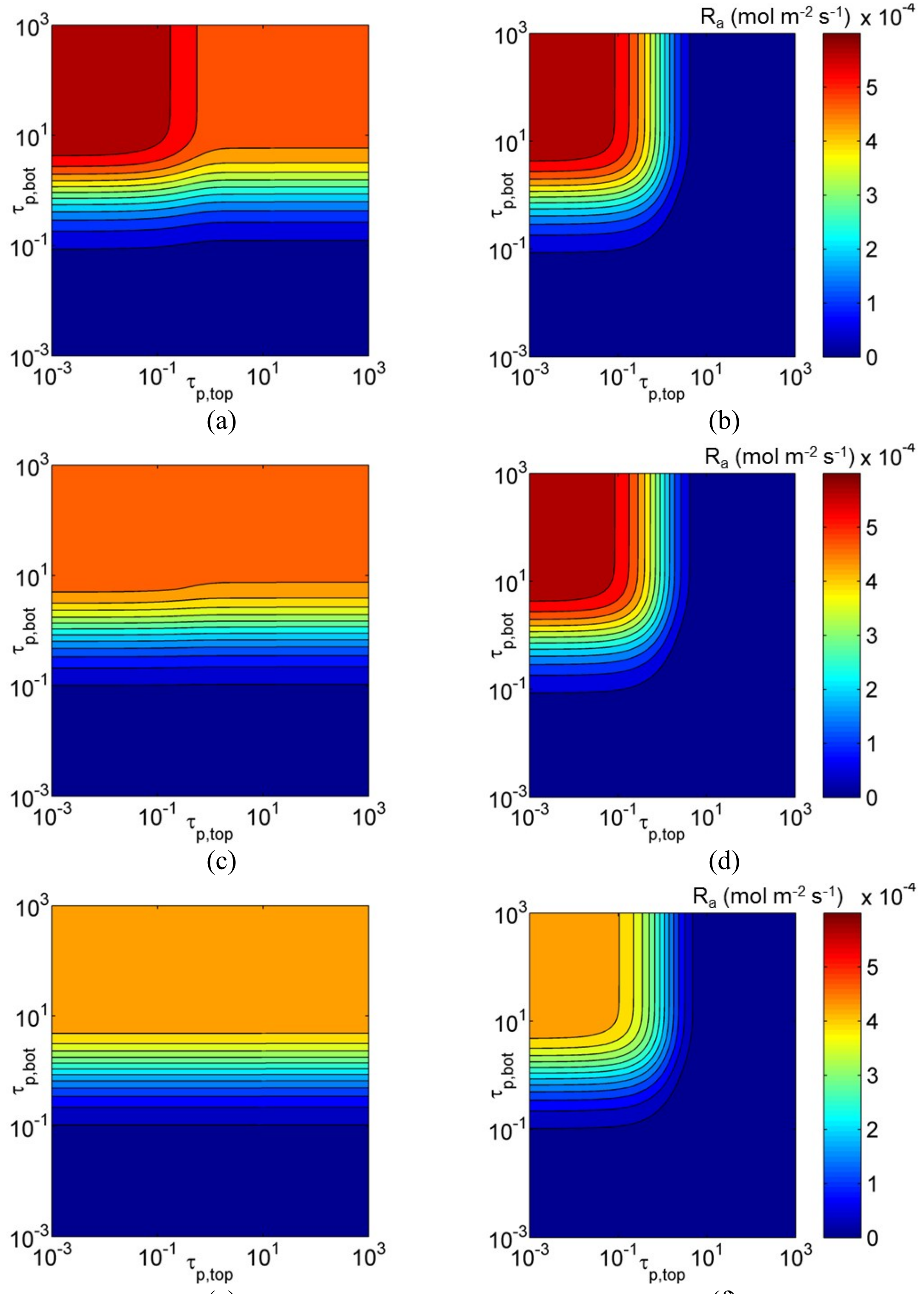

(a) (b)

(c) (d)

(e) (f)

Figure S3: Effect of particle optical thicknesses and redox shuttle concentrations on the bottom compartment (HER) reaction rates with (a,c,e) Option I (TiO_2 (OER) and $SrTiO_3$:Rh (HER)) and (b, d,f) Option II ($BiVO_4$ (OER) and $SrTiO_3$:Rh (HER)) with Q/QH_2 concentrations of (a,b)

10^{-3} M, (c,d) 10^{-2} M and (c,d) 0.1 M; $U_{L1} =- 0.53$ V and $U_{L2} = \ - 0.7\ V$ vs. *NHE* for all these cases.

Effect of Species Transport

Q/QH₂ redox shuttle

The concentration profiles of the redox shuttle species (Q/QH_2) and H^+ without diurnal illumination cycles are shown in Figure S4. For the same initial species concentrations considered in Figure 5, local depletion of p-benzoquinone occurs at $t = 70000$ s (or $t = 0.8$ days) in the bottom reaction compartment when the incident photon-flux is assumed to be constant. Figure S4(b) shows that with larger initial redox shuttle species concentrations, 0.65 M compared to 0.3 M, steady-state reactor operation can be achieved in this case. Similar to the results obtained with day/night variations in the incident photon flux, steady-state conditions are obtained after ~5 days of reactor operation, and the species transport is entirely driven by diffusion between the two reaction compartments.

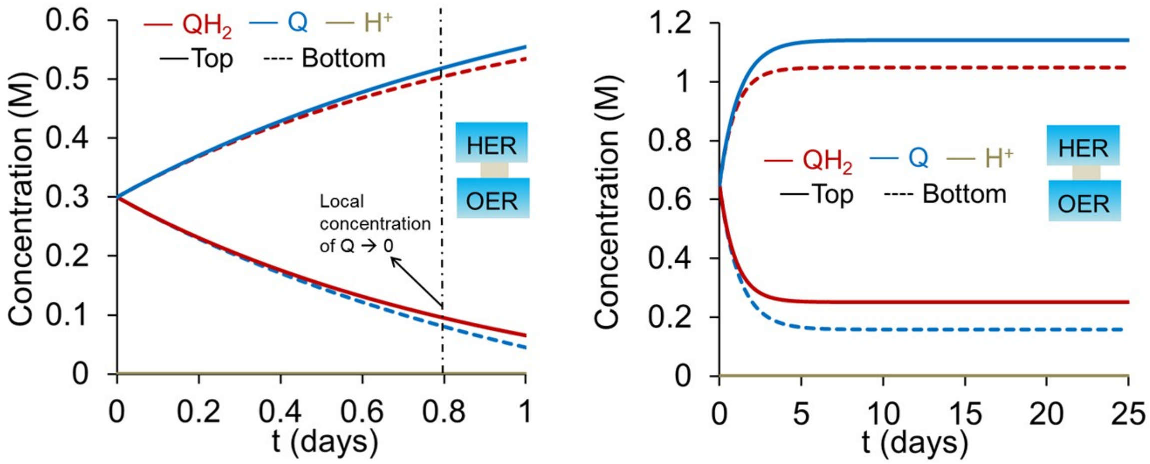

(a) (b)

Figure S4 Transient concentration profiles with Option II for 1 cm tall reaction compartments with $SrTiO_3$:Rh (top, HER) and $BiVO_4$ (bottom, OER) concentrations of 1.53×10^{-3} g L^{-1} and 2.12×10^{-3} g L^{-1} without diurnal illumination cycles and initial redox shuttle (Q/QH_2) concentrations of (a) 0.3 M and (b) 0.65 M.

IO_3^-/I^- redox shuttle

Similar to the Q/QH_2 redox shuttle, the IO_3^-/I^- redox shuttle also undergoes proton coupled electron transfer and exhibits pH independent thermodynamic potentials for the OER and the HER compartments.

$$I^- + 3H_2O + 6h\nu \rightarrow IO_3^- + 3H_2 \qquad E^0 = -1.085\ V$$

$$IO_3^- + 6h\nu \rightarrow I^- + \frac{3}{2}O_2 \qquad E^0 = -0.145\ V$$

A much lower reverse saturation current density, j_{rr} of 10^{-20} A m^{-2} compared to the baseline value of 10^{-15} A m^{-2}, was required for the $SrTiO_3$:Rh particles to yield the thermodynamic potential, 1.085 V, required to effect R_{ox} and HER. As both the oxidized and reduced forms of this shuttle do not absorb visible light, the non-linearities in the reaction rates due to concentration changes are not observed here. Figure S5 shows the transient concentration profiles of the redox couples for 1 and 10 cm tall reaction compartments at baseline STH efficiency of 1%. Steady-periodic operation is achieved in about 3 and 350 days for the 1 cm and 10 cm tall reaction compartments. The diffusion timescales to attain steady-periodic reactor operation exhibit a similar dependence on the reaction compartment heights, $t_{steady} \propto h^2$, as that of the Q/QH_2 redox shuttles due to the dominance of diffusive species transport over ionic migration. The mass-transfer overpotentials at baseline STH efficiency are 7 mV and 11 mV for the 1 and 10 cm tall reaction compartments respectively, and roughly a third of the magnitudes reported for the Q/QH_2 redox shuttle for the same reaction compartment heights. This scale factor arises because the IO_3^-/I^- redox shuttle undergoes a six-proton, six-electron transfer, whereas the Q/QH_2 redox shuttle undergoes a two-proton, two-electron transfer. The

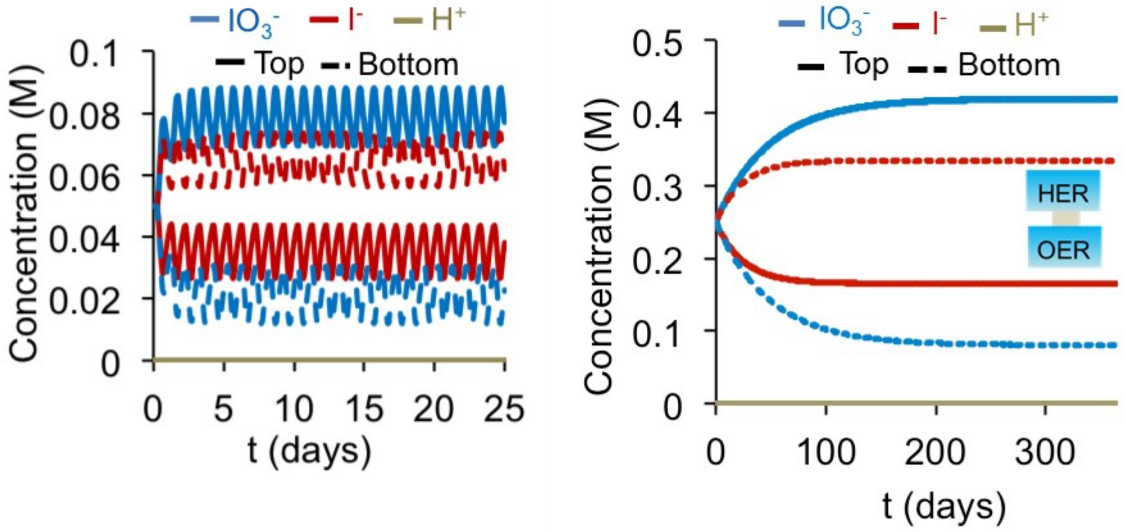

(a) (b)

Figure S5 Transient concentration profiles with the IO_3^-/I^- redox shuttle for reactor height, $SrTiO_3$:Rh (top, HER), $BiVO_4$ (bottom, OER) concentrations of (a) 1 cm, 0.8×10^{-3} g L^{-1}, 0.934×10^{-3} g L^{-1} and (b) 10 cm and 0.08×10^{-3} g L^{-1} and 0.091×10^{-3} g L^{-1}.

predicted redox species concentrations are well below the aqueous solubility limits of 9 M (KI) and 0.4 M (KIO_3) for both heights considered here. Sustained reactor operation with 1 cm tall reaction compartment is shown in Figure S6 for operation at 3.8% STH efficiency with this redox shuttle. The redox species concentrations are still maintained below their aqueous solubility limits, which makes this redox shuttle an attractive candidate for consideration in Z-scheme particle suspension reactor designs.

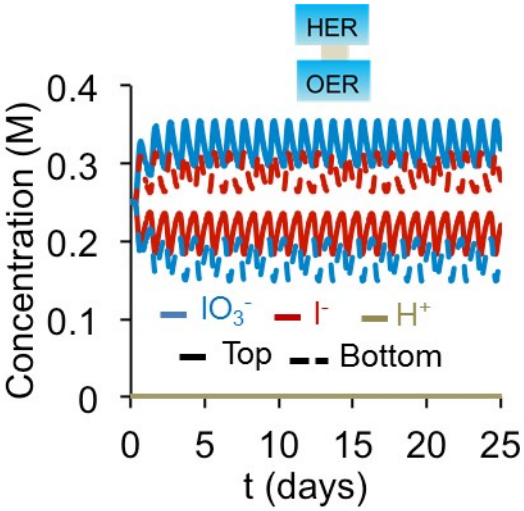

Figure S6 Transient concentration profiles with the IO_3^-/I^- redox shuttle for 1 cm tall reaction compartments, $SrTiO_3$:Rh (top, HER) and $BiVO_4$ (bottom, OER) concentrations of 3.3 × 10^{-3} g L^{-1} and 3.7 × 10^{-3} g L^{-1}

I_3^-/I^- and Fe^{3+}/Fe^{2+} redox shuttles

Figure S4 shows the transient concentration profiles for the redox species with the I^-/I_3^- and Fe^{2+}/Fe^{3+} redox shuttles for 0.1 cm tall reaction compartments. The initial species concentrations (0.04/0.06 M and 0.085/0.085 M for I_3^-/I^- and Fe^{3+}/Fe^{2+}, 0.008 M for H^+) were chosen to be the minimum values required for diffusion to sustain species transport between the reaction compartments for reaction rates consistent with 1% STH efficiency. Light attenuation by the redox shuttle species in the solution lowers the reaction rates of charge-carrier production/consumption in the reaction compartments to about 1.68×10^{-5} and 0.83×10^{-5} mol m^{-2} s^{-1} and (corresponding to 0.2% and 0.1% STH efficiency) for the I^-/I_3^- and Fe^{2+}/Fe^{3+} redox shuttles respectively. Due to the short lengthscale (0.1 cm) for species diffusion, steady-periodic reactor operation is attained within an hour, and therefore concentration profiles are identical even after the first day of reactor operation. Corresponding to the low reaction rates, the maximum change in

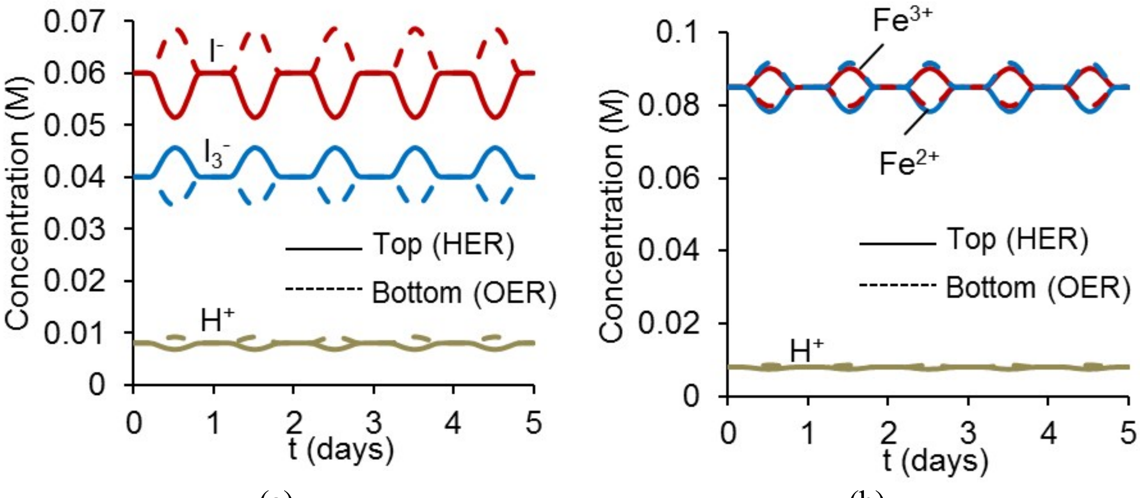

(a) (b)

Figure S7 Transient species concentration profiles with Option II, $SrTiO_3$:Rh (top, HER) and $BiVO_4$ (bottom, OER) particles in the top and bottom reaction compartments for (a) I_3^-/I^- and Fe^{2+}/Fe^{3+} redox shuttles for $h =$ 0.1 cm.

species concentrations from the initial values are 0.01 M for the I_3^-/I^- redox shuttles, and 0.06 M for the Fe^{3+}/Fe^{2+} redox shuttles. The proton concentration variation in a day (less than 0.001 M) is much lower, due to higher diffusivities in the aqueous suspension.

Effects of Reverse Saturation Current Densities

Sensitivity of the baseline reaction rates (Figures 5 and 6) to the reverse saturation current densities was evaluated, and the results are shown in Figure S8 for $h = 1\ cm$ and the Q/QH_2 redox shuttle. The reaction rates expected for reverse saturation current densities dictated by the Shockley–Queisser limit are predicted to be nearly equal to the baseline reaction rates, suggesting that increasing the sunlight-driven power production of the semiconductor particles, by further decreasing the reverse saturation current densities toward the detailed-balance limits, will not substantially alter the

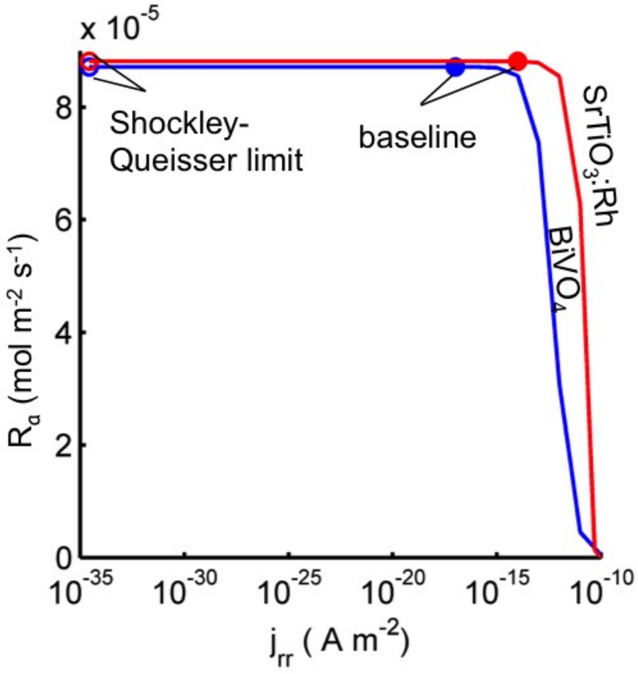

Figure S8 Effect of the reverse saturation current densities on the areal reaction rates for $SrTiO_3$:Rh (top, HER) and $BiVO_4$ (bottom, OER) particles; $h = 1$ cm and the concentrations of the Q/QH_2 redox shuttle are consistent with steady-periodic results (Figures 5 and 6) with fixed particle optical thicknesses of $\tau_{p,SrTiO_3:Rh} = 0.27$ and $\tau_{p,BiVO_4} = 0.38$.

performance. For a more than three-orders-of-magnitude increase in the reverse saturation current densities beyond the baseline values (10^{-18} A m^{-2} for $BiVO_4$ and 10^{-15} A m^{-2} for $SrTiO_3$:Rh particles), the reaction rates for each particle exponentially decreases (appears linear in Figure S8 because of the log-scale for j_{rr}). Over the full span of reverse saturation current densities considered, $BiVO_4$ exhibits a faster decline in the reaction rates as compared to $SrTiO_3$:Rh. This result is due to the differences in the OER and the HER catalytic parameters, where the smaller values of the Tafel slope for the OER result in a more abrupt increase the OER overpotential as a function of j_{rr}, and therefore it more rapidly approaches a reaction rate of nearly zero, at the condition of the open-circuit potential of the photodiode.

5. Nomenclature

Symbols

A	surface area, m^2
A_0	surface area of the particles per total suspension volume, m^{-1}
c	species concentration, mol m^{-3}
C	semiconductor particle concentration, g m^{-3}
d	diameter, m
D	diffusivity, m^2 s^{-1}
E	bandgap energy or band-edge energy locations, eV
E^0	thermodynamic potential at standard state versus *NHE*, V
f	fractional area coverage of the electrocatalyst on the photocatalyst particles
F	Faraday’s constant, 96500 C
ΔG	standard state free energy change, J mol^{-1}
g	volumetric absorption rate of photons, mol m^{-3} s^{-1}
h	reaction compartment height, m
I	radiation intensity, W m^{-2}
j	current density, A m^{-2}
j_0	exchange current density, A m^{-2}
N	species flux, mol m^{-2} s^{-1}
m	pertinent to number
n	pertinent to number of particles or electrons transferred
$\hat{n}$	unit normal vector
q_e	elementary charge, 1.6021 × 10^{-19} C
R_u	universal gas constant, 8.314 J mol^{-1} K^{-1}
R	reaction rate, mol m^{-2} s^{-1}
r	volumetric reaction rate, mol m^{-3} s^{-1}
T	temperature, K
t	time, s, or separator thickness, m
U	Nernstian potential, V
u	ionic mobility, m^2 s^{-1} V^{-1}
w	width of separator, m
x	x-coordinate, m
y	y-coordinate, m
y	spatial y-coordinate, m
z	charge magnitude

Greek

α	charge transfer coefficient
ε	separator porosity
$\bar{\epsilon}_\lambda$	spectral molar absorption coefficient, m^{-1} μm^{-1} M^{-1}
η	efficiency and overpotential, V
γ	diode quality factor

κ	absorption coefficient, m^{-1}
$\kappa_{p,\lambda}$	mass-specific spectral particle absorption cross-section, $m^2\ g^{-1}$
$\bar{\kappa}_{p,\lambda}$	photon-flux weighted particle absorption cross-section, $m^2\ g^{-1}$
ϕ	potential, V
Φ_λ	spectral incident photon flux, $m^{-2}\ \mu m^{-1}\ s^{-1}$
ρ	bulk density of particles, $kg\ m^{-3}$
τ	optical thickness

Subscripts

AM1.5	air mass 1.5 reference spectrum
a	pertinent to areal reaction rate and anodic reactions
avg	average value
back	pertinent to back reactions
bg	bandgap energy of the semiconductor
bot	pertinent to the bottom reaction compartment
c	pertinent to cathodic reactions
cat	pertinent to the catalyst
cb	pertinent to the conduction band
d	diode
eff	pertinent to effective value
e/h	pertinent to electrons and holes
HER	pertinent to the hydrogen evolution reaction
HOR	pertinent to the hydrogen oxidation reaction
i,j,k	pertinent to i^{th}, j^{th}, k^{th} species and reactions
max	pertinent to the maximum value
mt	pertinent to the mass transfer overpotential
OER	pertinent to the oxygen evolution reaction
ox	pertinent to the oxidation reaction
p	pertinent to particles
peak	peak value
ph	pertinent to photovoltage
rr	pertinent to reverse saturation current density
red	pertinent to the reduction reaction
STH	pertinent to solar-to-hydrogen efficiency
sel	pertinent to selective catalysis
sep	pertinent to the porous separator
sh	pertinent to the redox shuttle
top	pertinent to the top reaction compartment
unit	pertinent to the unit cell
vb	pertinent to the valence band

Other

AM1.5	air mass 1.5 reference spectrum for terrestrial solar insolation
PEC	photoelectrochemical
STH	solar-to-hydrogen
TMY3	typical meteorological data set

6. References

[1] S. Haussener, C. Xiang, J.M. Spurgeon, S. Ardo, N.S. Lewis, A.Z. Weber, Modeling, simulation, and design criteria for photoelectrochemical water-splitting systems, Energy Environ. Sci. 5 (2012) 9922. doi:10.1039/c2ee23187e.

[2] M.I. Cabrera, O.M. Alfano, A.E. Cassano, Absorption and Scattering Coefficients of Titanium Dioxide Particulate Suspensions in Water, J. Phys. Chem. 100 (1996) 20043–20050. doi:10.1021/jp962095q.

[3] V. Sivakumar, R. Suresh, K. Giribabu, V. Narayanan, BiVO 4 nanoparticles: Preparation, characterization and photocatalytic activity, Cogent Chem. 1 (2015) 1074647. doi:10.1080/23312009.2015.1074647.

[4] H. Kato, Y. Sasaki, N. Shirakura, A. Kudo, Synthesis of highly active rhodium-doped $SrTiO_3$ powders in Z-scheme systems for visible-light-driven photocatalytic overall water splitting, J. Mater. Chem. A. 1 (2013) 12327. doi:10.1039/c3ta12803b.

[5] R.O. Rahn, M.I. Stefan, J.R. Bolton, E. Goren, P.-S. Shaw, K.R. Lykke, Quantum yield of the iodide-iodate chemical actinometer: dependence on wavelength and concentrations., Photochem. Photobiol. 78 (2003) 146–52. http://www.ncbi.nlm.nih.gov/pubmed/12945582 (accessed June 29, 2016).

[6] M. Huwiler, H. Kohler, Pseudo-catalytic degradation of hydrogen peroxide in the lactoperoxidase/H_2O_2/iodide system, Eur. J. Biochem. 141 (1984) 69–74. doi:10.1111/j.1432-1033.1984.tb08158.x.

[7] V. Talrose, A.N. Yermakov, A.A. Usov, A.A. Goncharova, A.N. Leskin, N.A. Messineva, et al., UV/Visible Spectra, in: P.J. Linstrom, W.G. Mallard (Eds.), NIST Chem. WebBook, NIST Stand. Ref. Database Number 69, Gaithersburg, n.d. http://webbook.nist.gov.

[8] G.M. Hale, M.R. Querry, Optical Constants of Water in the 200-nm to 200-μm Wavelength Region, Appl. Opt. 12 (1973) 555. doi:10.1364/AO.12.000555.